Electronic Supplementary Material (ESI) for Energy & Environmental Science.

Electronic Supplementary Information

Monolithic heterojunction quasi-solid-state battery electrolytes based on thermodynamically immiscible dual phases

Sung-Ju Cho, [a‡] Gwan Yeong Jung, [a‡] Su Hwan Kim, [a] Minchul Jang, [b] Doo-Kyung Yang, [b] Sang Kyu Kwak, [a*] Sang-Young Lee[a*]

[a] Department of Energy Engineering, School of Energy and Chemical Engineering, Ulsan National Institute of Science and Technology (UNIST), Ulsan 44919, Korea

[b] Future Technology Research Center, LG Chem., Seoul 07796, Korea

* Corresponding author: Sang Kyu Kwak (skkwak@unist.ac.kr) and Sang-Young Lee (syleek@unist.ac.kr)

‡ These authors contributed equally to this work.

Theoretical Calculations:

Modeling and simulation details

DFT calculations. We performed DFT calculations to determine the optimized structures of the organic solvents (*i.e.*, EMS and TEGDME) and lithium salts (*i.e.*, LiTFSI) (Fig. S2a). Subsequently, because the organic solvents are known to form complex structures in the presence of Li^+ ions,[1,2] the most stable geometries of the complex structures for $[Li(EMS)_4]^+$ and $[Li(TEGDME)]^+$ were theoretically identified (Fig. S2b). $[Li(EMS)_4]^+$ formed a tetrahedral conformation, in which each oxygen atom of the EMS was coordinated with a Li^+ ion. In the case of $[Li(TEGDME)]^+$, a single Li^+ ion was coordinated with four oxygen atoms of TEGDME. All DFT calculations were performed using the DMol^3 program.[3,4] The B3LYP hybrid functional[5,6] was adopted for all calculations. Spin-polarized calculations were performed at the DNP 4.4 level. All electron relativistic effects were included in the core treatment. The convergence criterion of the self-consistent field was set to 1.0×10^{-6} Ha, and the geometry optimization was performed until the convergence criteria were satisfied (*i.e.*, 1.0×10^{-5} Ha for energy, 0.002 Ha/Å for force, and 0.005 Å for displacement).

MD simulations. We performed the MD simulations for each solvent (*i.e.*, EMS and TEGDME) and electrolyte (*i.e.*, EMS-EL;$[Li(EMS)_4][TFSI]$ and TEGDME-EL;[Li(TEGDME)][TFSI]) (1) to predict the miscibility by investigating the solubility parameters of bulk systems and (2) to observe the structural changes of the preformed interfaces of the solvent and electrolyte mixtures with various composition ratios. First, the optimized solvent and electrolyte molecules obtained via DFT calculations were packed in a periodic box to construct the bulk systems; the configuration information is presented in Table S1. The molar ratios between the organic solvents and lithium salts used in our simulations were taken from the experimental conditions (*i.e.*, 1:8 for LiTFSI:EMS and 1:1 for LiTFSI:TEGDME). In particular, the half portions of EMS molecules exist as complex structures (*i.e.*, $[Li(EMS)_4]^+$) by coordinating with Li^+ ions, while the remaining EMS molecules randomly exist in the 'EMS-EL' system. *NPT* (*i.e.*, isothermal-isobaric) MD simulations were initially performed for 300 ps to equilibrate the systems. Subsequently, *NVT* (*i.e.*, isothermal) MD simulations were performed to calculate the solubility parameters for each bulk system (Fig. S2c-f). Second, to investigate the immiscibility of preformed interfaces consisting of each solvent and electrolyte, four model systems were constructed with various composition ratios (*i.e.*, '4/6' for solvent mixture system, '3/7,' '5/5' and '7/3' for electrolyte mixture systems; Table S2. The solvent mixture system was constructed by eliminating the lithium salts from the '5/5' electrolyte mixture system to trace the effect of lithium salt on the immiscibility behaviors. All mixture systems were equilibrated by *NPT* MD simulations for 1 ns at room temperature and atmospheric pressure, followed by *NVT* MD simulations for 10 ns with a 1-fs time step (Fig. S3). All MD simulations were performed using the COMPASSII force field.[7,8] The temperature was controlled by a Nose-Hoover Langevin (NHL) thermostat,[9] and the pressure was controlled by a Berendsen barostat.[10] The Ewald scheme[11,12] and atom-based cutoff method (*i.e.,* a radius of 15.5 Å) were applied to treat electrostatic and van der Waals (vdW) interactions, respectively. All the partial atomic charges were defined using the COMPASSII force field.

Investigation of the miscibility based on calculated solubility parameters

To predict the miscibility of bulk systems of solvents and electrolytes, the solubility parameter (δ), which was defined by Hildebrand and Scott,[13] was calculated via MD simulations. The solubility parameter is defined by the square root of the cohesive energy density (CED), which is the average energy required to separate all molecules to an infinite distance from each other. The equation is specified as follows:

$$\delta = \sqrt{\frac{\Delta H_v - RT}{V_m}} = \sqrt{CED} \qquad (1)$$

where ΔH_v is the molar enthalpy of vaporization, R is the ideal gas constant, and V_m is the molar volume. Furthermore, the Hansen solubility parameter,[14] which is an extension of the Hildebrand solubility parameter (δ), was investigated to compare the relative strengths of dispersion (δ_d), polar (δ_p), and hydrogen bonding (δ_h) forces:

$$\delta^2 = {\delta_d}^2 + {\delta_p}^2 + {\delta_h}^2 = {\delta_{vdW}}^2 + {\delta_{ES}}^2 \qquad (2)$$

In this study, the dispersion forces (δ_d) were referred as vdW forces (δ_{vdW}). Additionally, because the hydrogen bonding forces were negligible in our system, polar (δ_p) and hydrogen bonding forces (δ_h) were combined into electrostatic forces (δ_{ES}).

Structural analysis based on the demixing index and interaction energy

To estimate the degree of immiscibility of solvent and electrolyte mixtures at a specific time, the "demixing index" (χ_{demix}), which was previously defined by Muzet *et al.*,[15] was calculated via MD simulations. Initially, the simulation box was partitioned into '*n*' equal boxes with a width of approximately 1.6 Å (*i.e.*, *n* ranges from 40 to 70). For each box *i*, the number density (d_i) corresponding to each solvent and electrolyte was estimated. Subsequently, the inverse density $1/d_i$ of each box *i* was calculated by summing the reciprocal number density of each component as follows.

$$1/d_i = 1/d_{EMS,i} + 1/d_{TEGDME,i} \ (i.e., \text{ solvent mixture, } i \text{ ranges from 1 to } n) \qquad (3)$$

$$1/d_i = 1/d_{[EMS-EL],i} + 1/d_{[TEGDME-EL],i} \ (i.e., \text{ electrolyte mixture, } i \text{ ranges from 1 to } n) \qquad (4)$$

Finally, χ_{demix} was obtained by averaging d_i over all boxes and dividing by the normalization factor (N) as follows,

$$\chi_{demix} = \frac{1}{N}\langle d_i \rangle \qquad (5)$$

where χ_{demix} is ranged from 0.0 (for totally separated phases) to 1.0 (for perfectly mixed phase). The time evolutions of χ_{demix} for solvent and electrolyte mixtures are shown in Fig. 1d. In addition, the interaction energy (ΔE_{int}) between two phases at the interface was calculated as follows,

$$\Delta E_{int} = E_{total} - E_{\boldsymbol{A}} - E_{\boldsymbol{B}} \ (\boldsymbol{A} = \text{EMS or EMS-EL, } \boldsymbol{B} = \text{TEGDME or TEGDME-EL}) \qquad (6)$$

where E_{total} is the total potential energy of each solvent and electrolyte system, E_A is the total potential energy of EMS or EMS-EL, and E_B is the total potential energy of TEGDME or TEGDME-EL. The relative changes of the interaction energy (ΔE_{int}) relative to its initial value were monitored as a function of time (Fig. 1d).

Interfacial tension calculation

The interfacial tension (γ) was calculated using pressure tensors as follows.[16]

$$\gamma = \frac{1}{2} L_z \left[P_{zz} - \frac{1}{2}(P_{xx} + P_{yy}) \right] \quad (7)$$

where P_{zz} is the pressure tensor in the *z*-direction (*i.e.*, normal to the interface); P_{xx} and P_{yy} are the pressure tensor in the *x*- and *y*-directions (*i.e.*, horizontal to the interface), respectively; and L_z denotes the box length in the *z*-direction (Fig. 1c). The average values of the interfacial tensions obtained from MD simulations are shown in Table S3.

Methods:

Design and fabrication of the MH-QEs.

In the first step of the fabrication of the MH-QEs, the QE precursor, which consisted of an ionic medium (1 M LiTFSI in EMS or 2.3 M LiTFSI in TEGDME), a UV-curable ETPTA monomer (incorporating 1.0 wt% HMPP as a photoinitiator) and Al_2O_3 nanoparticles (average particle size ~ 300 nm), was prepared. The composition ratio of the QE precursor was ionic medium/ETPTA/Al_2O_3 = 34/6/60 (w/w/w). The EMS-based QE precursor was directly printed on a sulfur cathode. During the printing process, the EMS-based QE precursor infiltrated into the interstial voids of the sulfur cathode along with formation of the cast layer. Subsequently, the ETPTA monomers in the EMS-based QE precursor were crosslinked after exposure to the UV curing, yielding the solidified EMS-QEs.

Details regarding the UV curing-assisted printing process and rheological understanding were described in our previous publications.[17,18] The UV irradiation was performed using a Hg UV-lamp (Lichtzen) with an irradiation peak intensity of approximately 2000 mW cm^{-2} on the sample surface. Subsequently, on the top of the EMS-QE, the TEGDME-QE was introduced via the same printing and UV curing process, resulting in the formation of the MH-QE on the sulfur cathode.

Characterizations. The dissolution behavior of the polysulfide intermediate (0.1 M Li_2S_8)[19] in the EMS-EL and TEGDME-EL was quantitatively investigated as a function of time using UV-vis spectrophotometry (Cary 5000, Agilent) spectroscopy. The ^{1}H NMR spectra were recorded on an 400 MHz AVANCE III HD instrument (Bruker) in CD_3OD. The chemical shifts were referenced to the protio-solvent impurities (δ 3.31 ppm (CD_2HOD)) and were reported in ppm. The UV curing reaction of the ETPTA polymer skeleton in the MH-QE was examined using FT-IR spectroscopy (Varian 660-IR, Varian Medical Systems). The morphologies of the samples were characterized using FE-SEM (S-4800, HITACHI) and energy dispersive X-ray spectroscopy (EDS). After the cycling test, the lithium anodes were extracted from the cycled cells without being washed in an argon-filled glove box and transferred to the XPS spectrometer right away to avoid hydrolysis or oxidation of Li_2S and lithium polysulfides. The XPS (Thermo Fisher) was performed with focused monochromatized Al Kα radiation. The Raman spectra were obtained using an Alpha 300S (WITec) with a 532-nm laser.

Electrochemical measurements. The sulfur cathode (areal sulfur loading = 1.2 mg cm^{-2}) was prepared with a composition ratio of sulfur/carbon black/SBR-CMC binder = 75/20/5 (w/w/w) and then vacuum-dried for one day at 50 °C. A coin-type (CR2032) cell was fabricated by assembling the sulfur cathode, MH-QE and lithium foil anode in an argon-filled glove box. The electrochemical properties of the cells were investigated using a cycle tester (PNE Solution Co., Ltd, Korea) under various discharge/charge conditions at constant temperature (25 °C). The EIS data for the cells were recorded using a potentiostat/galvanostat (VSP classic, Bio-Logic) in the frequency range from 10^{-2} to 10^6 Hz with an applied voltage of 10 mV. The shuttle factor equation was given as $f = K_s \cdot Q_H[S_{total}]/I$, where K_s is the heterogeneous reaction constant related to polysulfide diffusion and reaction, Q_H is the theoretical charge/discharge capacity of the high plateau, and I is the charge/discharge current. [S_{total}] is assumed to be the polysulfide amount required for the full conversion of sulfur.

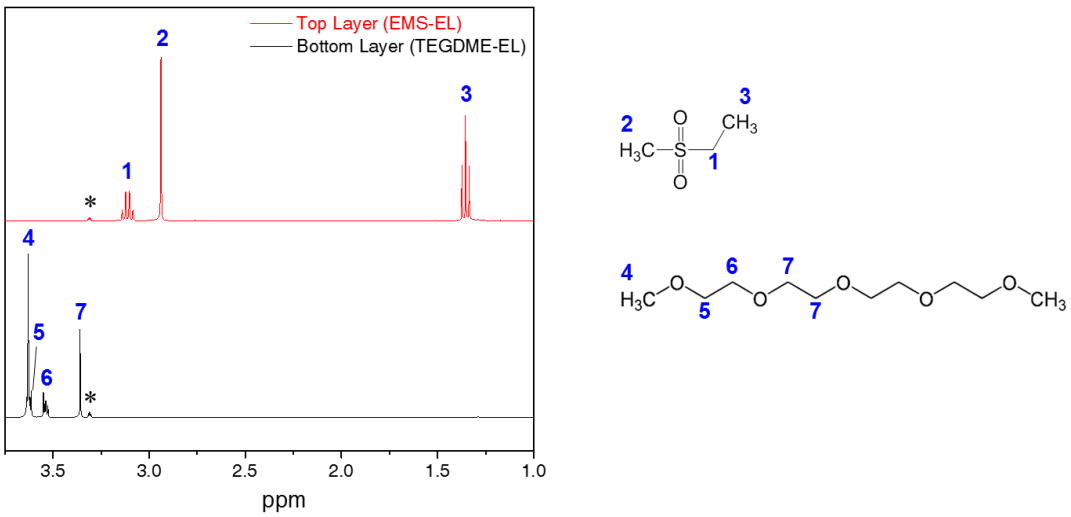

Fig. S1 ^{1}H NMR spectra of the top and bottom layers in electrolyte mixtures (EMS-EL/TEGDME-EL = 5/5 (v/v), shown in Fig. 1a). (∗ indicates the residual solvent peak.)

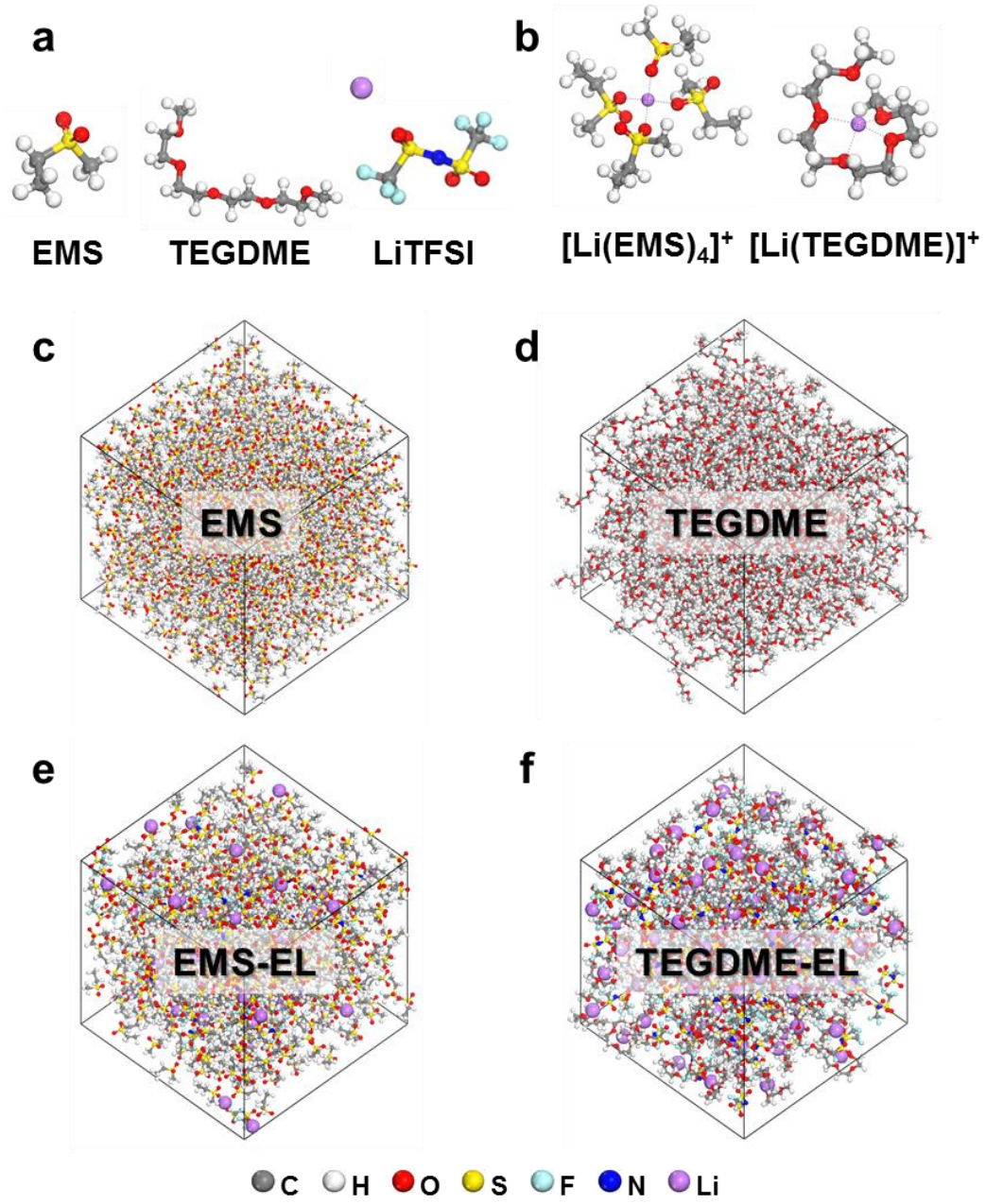

Fig. S2 Model systems used for the solubility parameter (δ) calculation. (a) Molecular structures of EMS, TEGDME, and LiTFSI. (b) Complex structure of $[Li(EMS)_4]^+$ and $[Li(TEGDME)]^+$. (c-f) Bulk models of (c) EMS (d) TEGDME (e) $[Li(EMS)_4][TFSI]$ (*i.e.*, EMS-EL) (f) [Li(TEGDME)][TFSI] (*i.e.*, TEGDME-EL). Carbon, hydrogen, oxygen, sulfur, fluorine, nitrogen, and lithium atoms are shown in gray, white, red, yellow, cyan, blue, and purple, respectively.

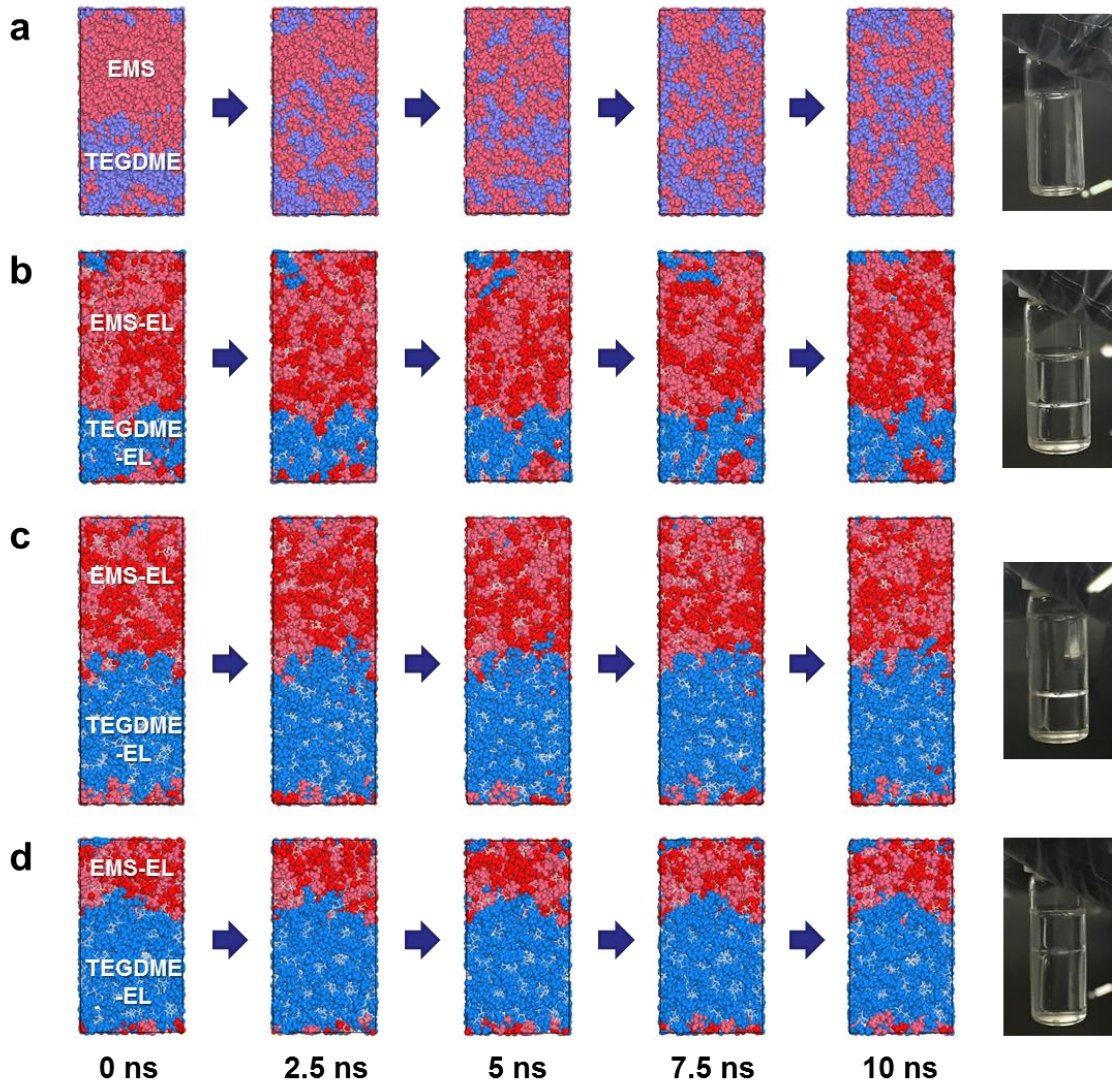

Fig. S3 MD simulation snapshots of the solvent and electrolyte mixtures as a function of time and the corresponding photographs. (a) Solvent mixture (EMS/TEGDME). (b-d) Electrolyte mixtures (b)EMS-EL/TEGDME-EL = 3/7, (c) 5/5, (d) 7/3. EMS, TEGDME, $[TFSI]^-$, $[Li(EMS)_4]^+$, and $[Li(TEGDME)]^+$ are shown in pink, purple, gray, red, and blue, respectively.

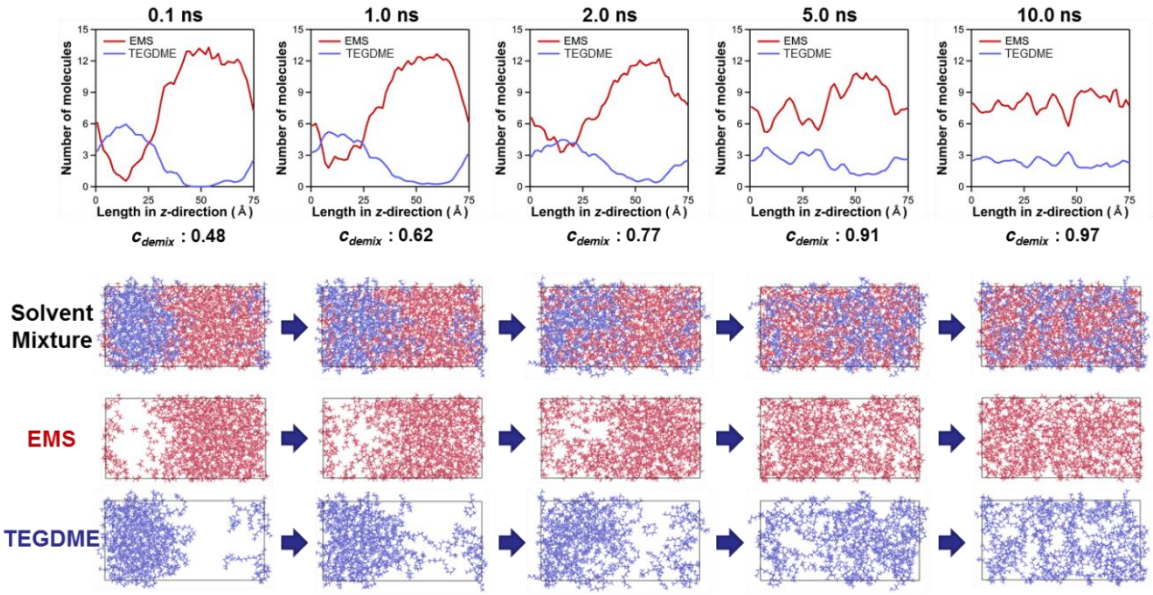

Fig. S4 Concentration profiles and MD simulation snapshots of the solvent mixture as a function of time. For clarity, EMS and TEGDME are separately visualized the mixture system. EMS and TEGDME are shown in pink and purple, respectively. Note that the *z*-axis is perpendicular to the interface.

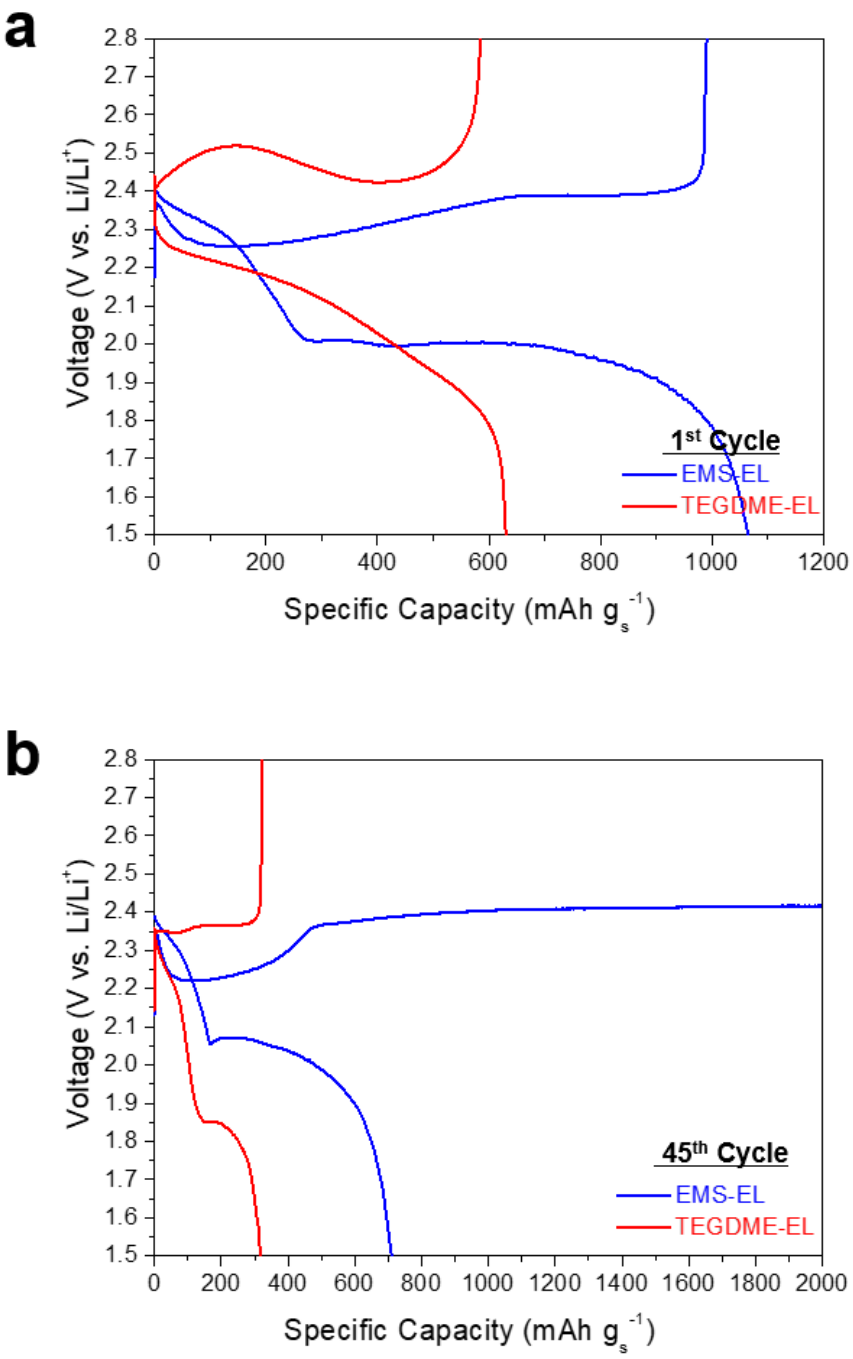

Fig. S5 Charge/discharge profiles of the Li-S cells containing the EMS-EL and TEGDME-EL. The cells were examined at a charge/discharge current density of 0.1 C/0.1 C under a voltage range of 1.5–2.8 V. (a) 1st cycle. (b) 45th cycle.

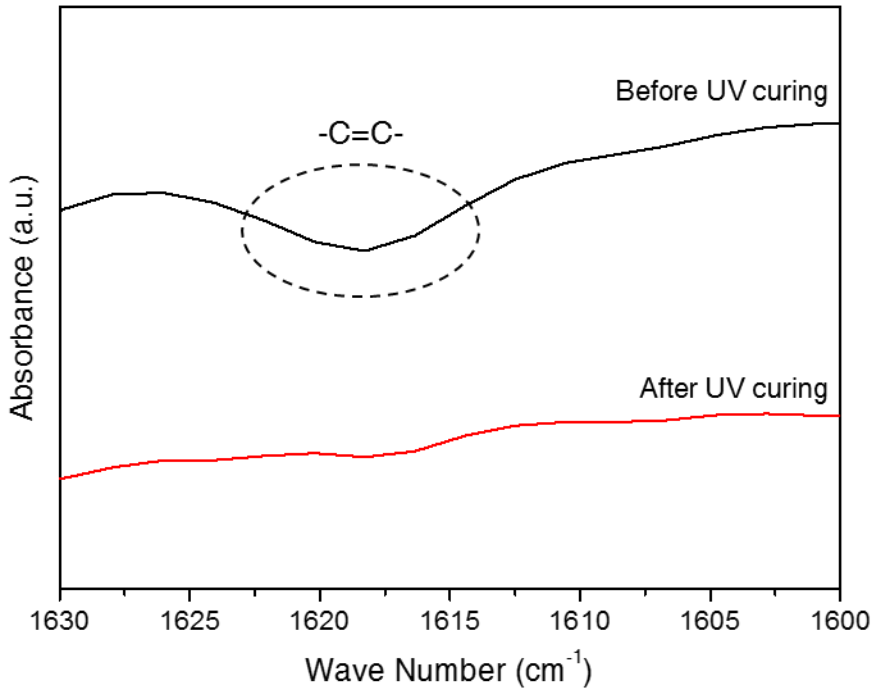

Fig. S6 Changes in the FT-IR spectra of the acrylic C=C double bonds of the ETPTA polymer before/after UV curing.

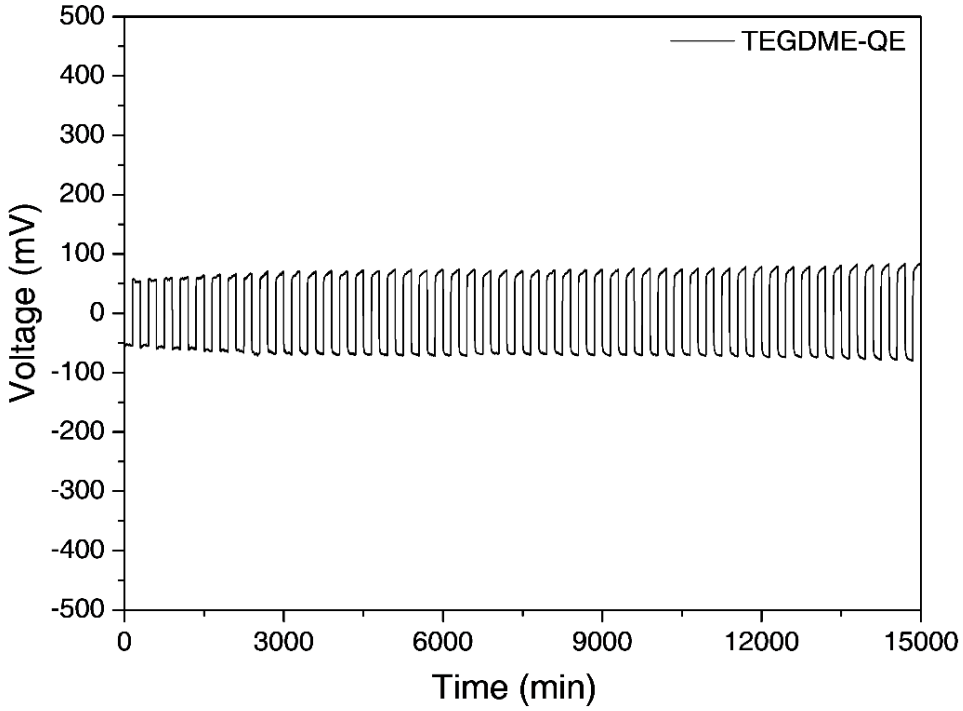

Fig. S7 Time evolution of the cell voltage of a symmetric cell (lithium metal/TEGDME-QE/lithium metal) with a cycling capacity of 0.5 mAh cm^{-2} at a current density of 0.1 mA cm^{-2}.

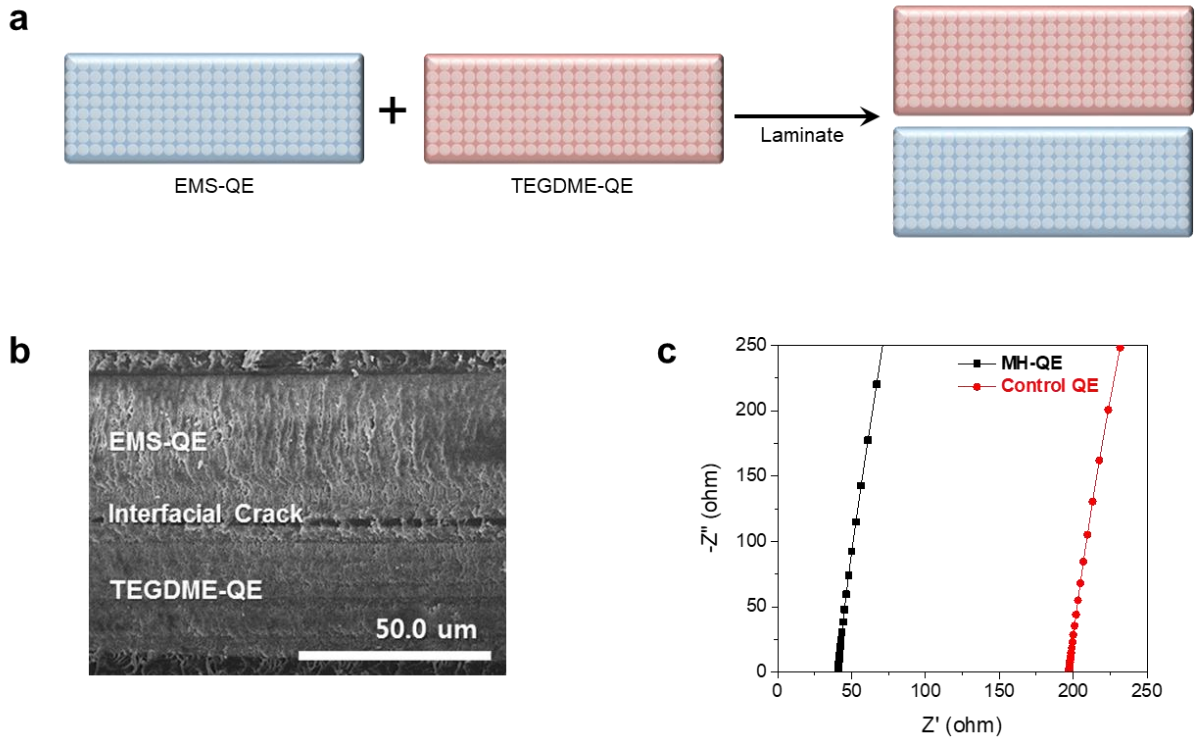

Fig. S8 (a) Schematic representation depicting the fabrication of the control QE (that was prepared by simply stacking the EMS-QE film with the TEGDME-QE film). (b) Cross-sectional SEM image of the control QE. Interfacial cracks between the two QE films were clearly observed. (c) AC impedance spectra of the MH-QE and control QE at 30°C. This measurement was conducted using a coin-type cell (CR2032), in which the stack pressure was applied to the electrolytes.

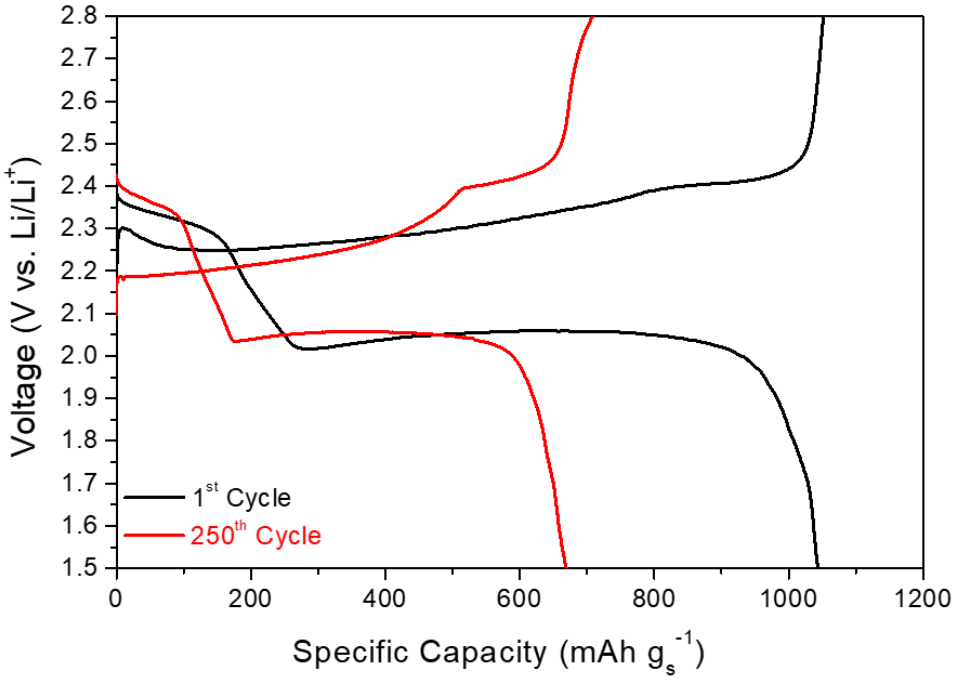

Fig. S9 Charge/discharge profiles (1st and 250th cycles) of the Li-S cells containing the MH-QE. The cells were examined at a charge/discharge current density of 0.1 C/0.1 C under a voltage range of 1.5–2.8 V.

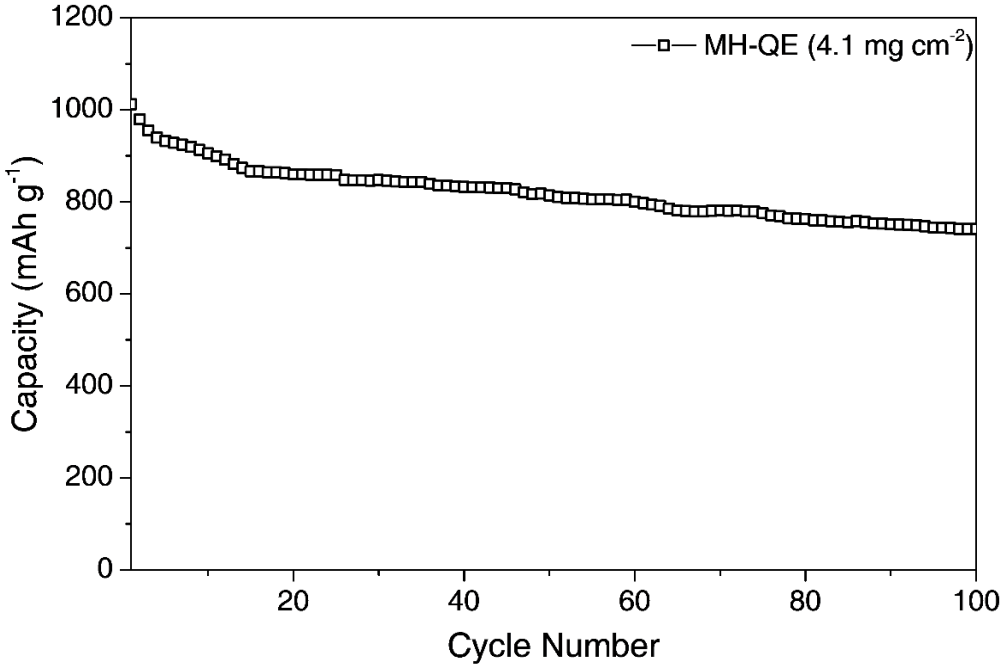

Fig. S10 Cycling performance of the Li-S cells containing the MH-QE (areal mass loading of the sulfur cathode = 4.1 mg cm^{-2}). The cells were examined at a charge/discharge current density of 0.1 C/0.1 C under a voltage range of 1.5–2.8 V.

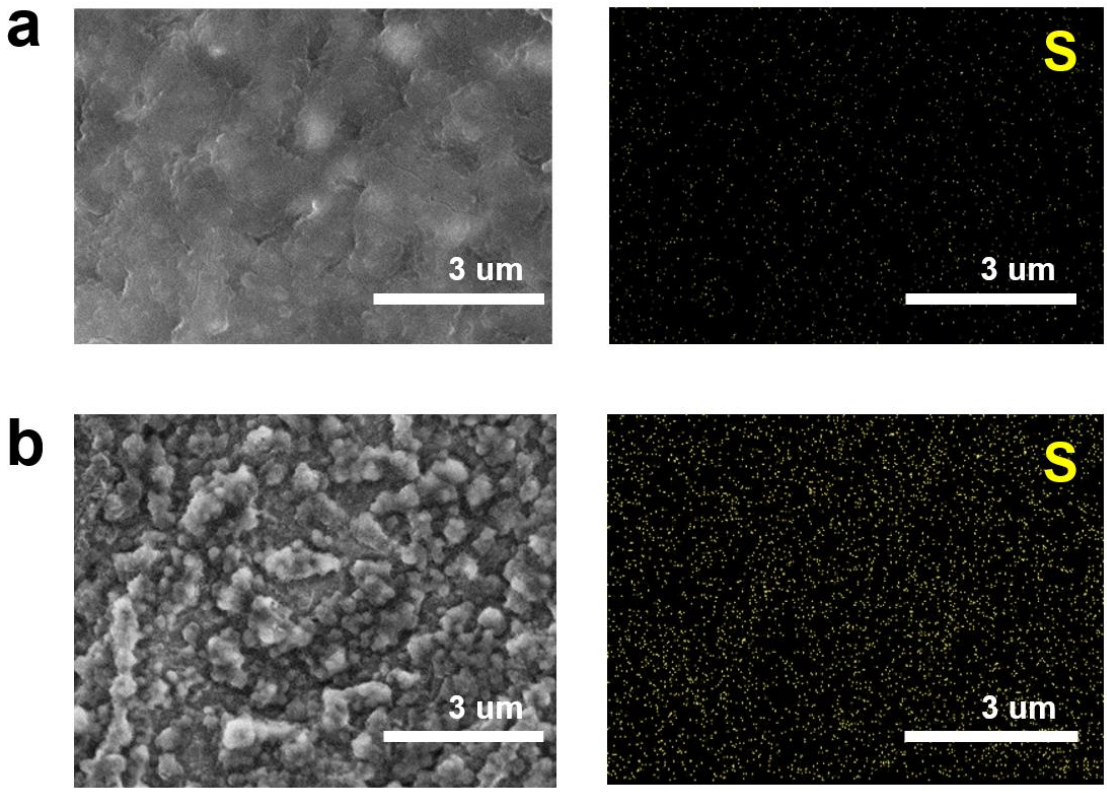

Fig. S11 SEM images (left column, in Fig. 3b) and EDS sulfur mapping images (right column) of the lithium anodes at DOD 100% after 250 cycles: (a) MH-QE, (b) DOL/DME.

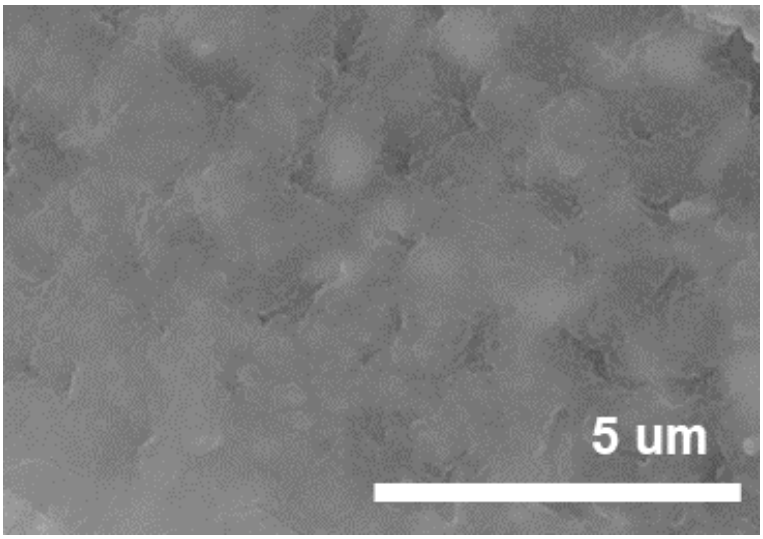

Fig. S12 SEM image of the lithium metal anode surface after 1st cycle for MH-QE.

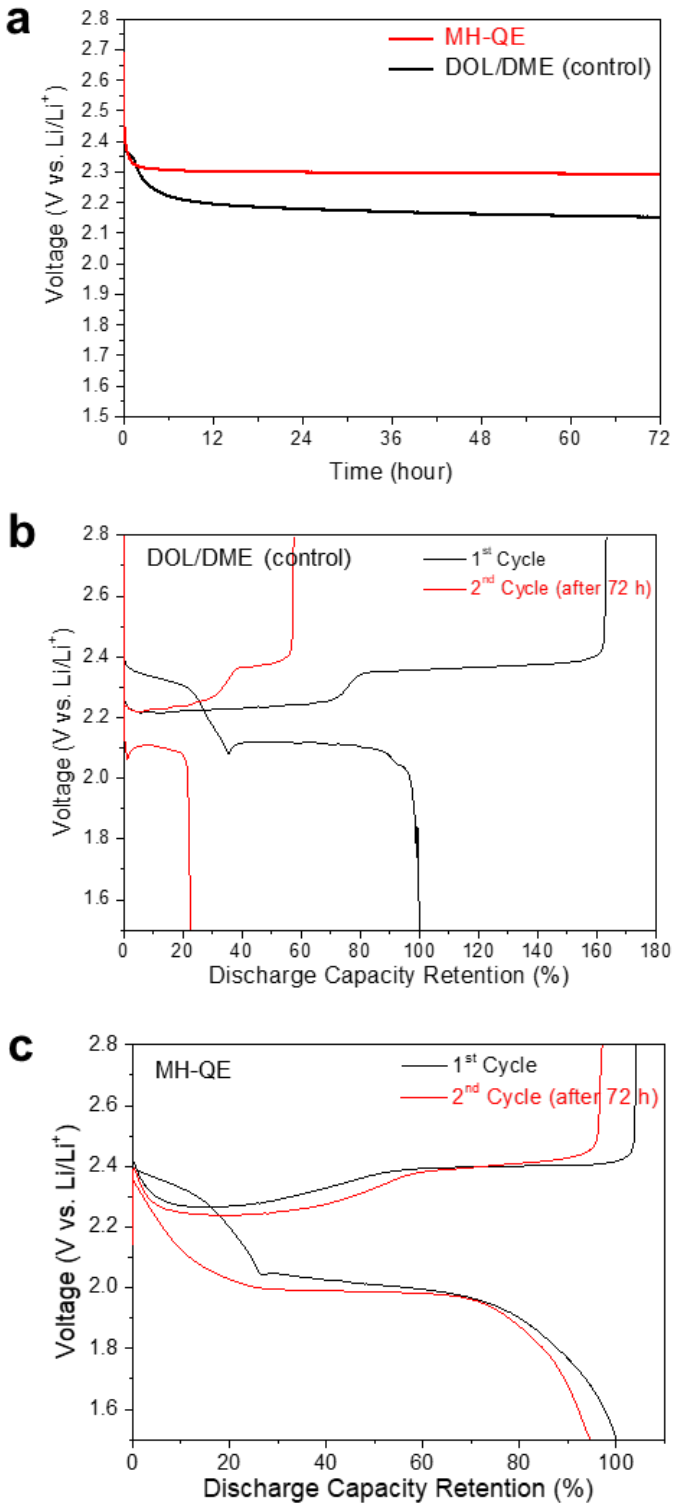

Fig. S13 Self-discharge behavior of the Li-S cells assembled with the MH-QE and DOL/DME. (a) OCV profiles as a function of the elapsed time. (b,c) Charge/discharge profiles before/after an elapsed time of 72 h: (b) DOL/DME. (c) MH-QE.

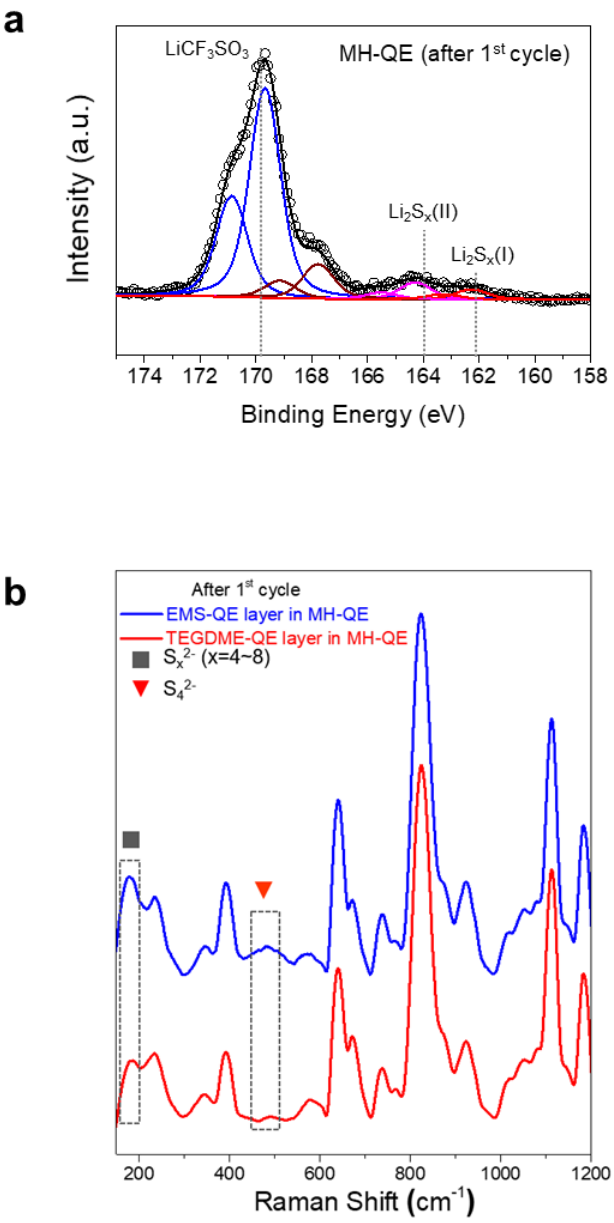

Fig. S14 Structural characterization of the lithium metal anodes after 1st cycle (for MH-QE). (a) S 2p XPS spectra, in which the Li-S cells were fully discharged. (b) Raman spectra, in which the MH-QE was taken at a cell voltage of 2.1 V.

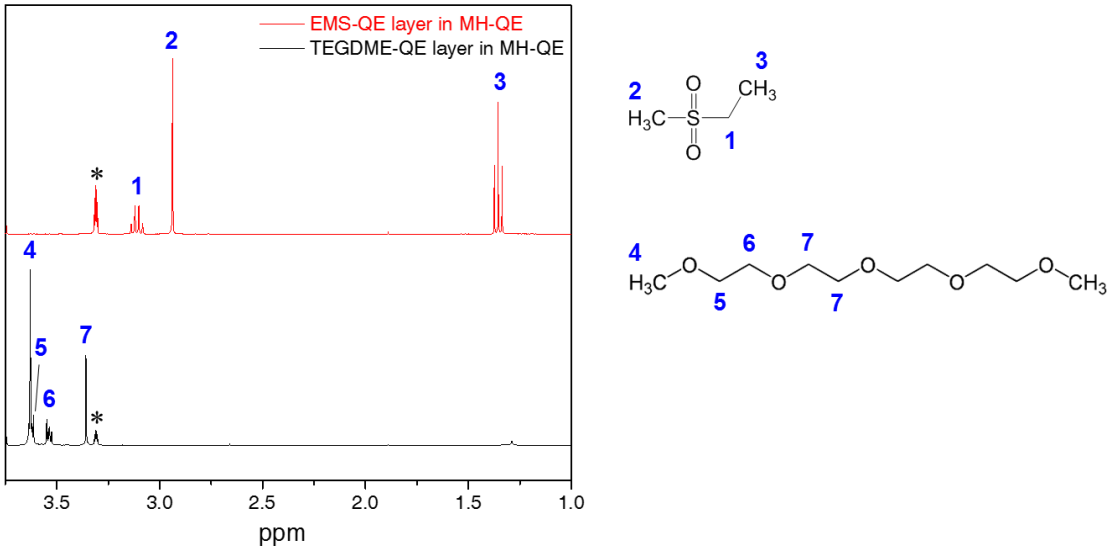

Fig. S15 ^{1}H NMR spectra of the EMS-QE and TEGDME-QE layers in the MH-QE after 250 cycles. (∗ indicates residual solvent peaks.)

Table S1. Summary of the bulk systems used in the MD simulations. The total number of molecules (*i.e.*, EMS, TEGDME, and LiTFSI), number of atoms, and box size are included.

	EMS	**TEGDME**	**EMS-EL**	**TEGDME-EL**
EMS	1000	-	400	-
TEGDME	-	300	-	100
LiTFSI	-	-	50	100
Total number of atoms	14000	11100	6400	5300
Box size (Å^3)	55.5×55.5×55.5	47.4×47.4×47.4	42.2×42.2×42.2	38.5×38.5×38.5

Table S2. Summary of the solvent mixture and electrolyte mixture systems used in MD simulations. '3/7,' '5/5,' and '7/3' represent the composition ratios of the electrolyte mixtures (v/v). The experimental and calculated values of the composition ratio, total number of molecules (*i.e.*, EMS, TEGDME, and LiTFSI), number of atoms, and box size are included.

	Electrolyte Mixture			Solvent Mixture
	3/7	**5/5**	**7/3**	
Composition ratio (v:v)	0.27 : 0.73	0.47 : 0.53	0.67 : 0.33	0.38 : 0.62
EMS	400	400	160	400
TEGDME	50	117	109	117
LiTFSI	100	167	129	-
Total number of atoms	9050	12601	8337	9929
Box size (Å^3)	35.9×35.9×79.9	36.0×36.0×109.9	36.4×36.4×68.8	38.0×38.0×75.5

Table S3. Theoretical calculation of interfacial tensions (γ) of the solvent mixture and electrolyte mixture. The solvent mixture (EMS/TEGDME) and electrolyte mixtures with different composition ratios (EMS-EL/TEGDME-EL = 3/7, 5/5, and 7/3 (v/v)) were investigated; P_{xx}, P_{yy}, and P_{zz} represent the pressure tensors along the *x*-, *y*-, and *z*-directions. Note that the *z*-axis is perpendicular to the interface.

	P_{xx} (MPa)	P_{yy} (MPa)	P_{zz} (MPa)	γ (dyne/cm)
Electrolyte Mixture (EMS-EL/TEGDME-EL)				
3 / 7	1.34	-1.15	5.47	21.48
5 / 5	10.31	15.18	23.32	58.12
7 / 3	6.46	10.23	15.53	24.71
Solvent Mixture (EMS/TEGDME)	-17.03	-17.77	-16.09	4.92

Table S4. Comparison of various electrolyte approaches for Li-S cells in terms of cycling performance. (LiOTf: Lithium trifluromethanesulfonate (triflate), LiBETI: Lithium bis(pentafluoroethanesulfonyl)imide, DEGDME: diethylene glycol dimethyl ether, DEC: Diethyl carbonate, PYR14: 1-Buthyl-1-methyl-pyrrolidinium, EMIM: 1-Ethyl-3-methyl-imidazolium, PP13: 1-Propyl-1-methyl-piperidinium)

	Electrolyte	Current density	Capacity/Cycle life	Ref
Solvent	1 M LiOTf in TEGDME	1/16 C	~ 330/50	20
	1 M LiOTf in TEGDME/DOL		~500/50	
	1 M LiOTf in DME/DEGDME		~400/50	
	1 M LiTFSI in DOL	0.1 C	~210/10	21
	1 M LiTFSI in DOL/TEGDME		~260/10	
	1 M LiTFSI in TEGDME		~430/10	
	1 M LiOTf in TEGDME	100mA/g discharge 500mA/g charge	~380/10	22
	1 M LiOTf in DOL/DME		~750/10	
	1 M LiOTf in EMS/DEC (8:1)		~20/10	
	1 M LiOTf in EMS/DOL/DME (4:1:1)		~410/10	
Salt	1 M LiOTf in DME/DOL (4/1,v/v)	0.5 C	~0/55	23
	1 M LiTFSI in DME/DOL (4/1,v/v)		~750/55	
	1 M LiBETI in DME/DOL (4/1,v/v)		~720/55	
	1 M $LiPF_6$ in DME/DOL (4/1,v/v)		~600/55	
	2 M LiTFSI in DOL/DME	0.2 C	~400/100, (CNT/S) ~220/100, (KB/S)	24
	7 M LiTFSI in DOL/DME		~780/100, (CNT/S) ~600/100, (KB/S)	
Additive	0.5 M LiOTf in DOL/TEGDME	0.1 mA/cm^2	~ 200/50	25
	0.5 M LiOTf in DOL/TEGDME + 0.4 M $LiNO_3$		~500/50	
	1 M LiTFSI in TEGDME/DOL(33/67, v/v)	0.1 C	~ 500/20	26
	1 M LiTFSI in TEGDME/DOL(33/67, v/v) + 0.01 M $LiNO_3$		~450/20	
	1 M LiTFSI in TEGDME/DOL(33/67, v/v) + 0.2 M $LiNO_3$		~600/20	
	1 M LiTFSI in TEGDME	0.1 C	~ 300/40	27
	1 M LiTFSI in TEGDME + 5 wt% Li_2S/P_2S_5		~900/40	
Ionic Liquid	PYR14TFSI + 0.2 M LiTFSI in TEGDME	0.054 mA/cm^2	~440/20	28
	1 M LiTFSI in EMITFSI	50 mA/g	~500/40	29
	1 M LiTFSI in PP13TFSI	0.1 C	~320/10	30
	Li(TEGDME)TFSI	139 mA/g	~720/50	31
	MH-QE	0.1 C	864/10 831/20 754/50 703/100 700/250	This study

References

1 K. Xu, *Chem. Rev.*, 2004, **104**, 4303-4417.

2 K. Ueno, R. Tatara, S. Tsuzuki, S. saito, H. Doi, K. Yoshida, T. Mandai, M Matsugami, Y. Umebayashi, K. Dokko, M. Watanabe, *Phys. Chem. Chem. Phys.*, 2015, **17**, 8248-8257.

3 B. Delley, *J. Chem. Phys.*, 1990, **92**, 508-517.

4 B. Delley, *J. Chem. Phys.*, 2000, **113**, 7756-7764.

5 A. D. Becke, *J. Chem. Phys.*, 1993, **98**, 5648-5652.

6 P. J. Stephens, F. J. Devlin, C. F. Chabalowski, M. J. Frisch, *J. Phys. Chem.*, 1994, **98**, 11623-11627.

7 H. Sun, *J. Phys. Chem. B*, 1998, **102**, 7338-7364.

8 H. Sun, *Comput. Theor. Polym. Sci.*, 1998, **8**, 229-246.

9 A. A. Samoletov, C. P. Dettmann, M. A. J. Chaplain, *J. Stat. Phys.*, 2007, **128**, 1321-1336.

10 H. J. C. Berendsen, J. P. M. Postma, W. F. van Gunsteren, A. DiNola, J. R. Haak, *J. Chem. Phys.*, 1984, **81**, 3684-3690.

11 P. P. Ewald, *Ann. Phys.*, 1921, **369**, 253-287.

12 M. P. Tosi, *Solid State Phys.*, 1964, **16**, 1-120.

13 J. H. Hildebrand, R. L. Scott, The solubility of nonelectrolytes. *Reinhold Pub. Corp.* USA 1950, p. 253.

14 C. M. Hansen, *J. Paint Technol.*, 1967, **39**, 104-117.

15 N. Muzet, E. Engler, G. Wipff, *J. Phys. Chem. B*, 1998, **102**, 10722-10788.

16 J. S. Rowlinson, B. Widom, Molecular theory of capillarity. Wiley-VCH, Weinheim, Germany 1982, p. 327.

17 S. H. Kim, , K. H. Choi, S. J. Cho, S. Choi, S. Park, S. Y. Lee, *Nano Lett.*, 2015, **15**, 5168-5177.

18 E. H. Kil, K. H. Choi, H. J. Ha, S. Xu. J. A. Rogers, M. R. Kim, Y. G. Lee, K. M. Kim, K. Y. Cho, S. Y. Lee, *Adv. Mater.*, 2013, **25**, 1395-1400.

19 R. D. Rauh, F. S. Shuker, J. M. Marston, S. B. Brummer, *J. Inor. Nucl. Chem.*, 1977, **39**, 1761-1766.

20 J.-W. Choi, J.-K. Kim, G. Cheruvally, J.-H. Ahn, H.-J. Ahn, K.-W. Kim, *Electrochim. Acta.*, 2007, **52**, 2075-2082.

21 C. Barchasz, J.-C. Lepretre, S. Patoux, F. Alloin, *J. Electrochem. Soc.*, 2013, **160**, A430-A436.

22 J. Gao, M. A. Lowe, Y. Kiyam H. D. Abruna, *J. Phys. Chem. C*, 2011, **115**, 25132-25137.

23 S. Kim, Y. Jung, S.-J. Park, *Electrochim. Acta*, 2007, **52**, 2116-2122.

24 K. Suo, Y.-S. Hu, H. Li, M. Armand, L. Chen, *Nat. Commun.*, 2013, **4**, 1481.

25 X. Liang, Z. Wen, Y. Liu, M. Wu, J. Jin, H. Zhang, Z. Wu, *J. Power Sources.*, 2011, **196**, 9839-9843.

26 H. S. Kim, T.-G. Jeong, N.-S. Choi, Y.-T. Kim, *Ionics*, 2013, **19**, 1795-1802.

27 Z. Lin, Z. Liu, W. Fu, N. J. Dudney, C. Liang, *Adv. Funct Mater.*, 2013, **23**, 1064-1069.

28 J. H. Shin, E. J. Cairns, *J. Electrochem. Soc.*, 2008, **155**, A368-A373.

29 J. Wang, S. Y. Chew, Z. W. Zhao, S. Ashraf, D. Wexler, J. Chen, S. H. Ng, S. L. Chou, H. K. Liu, *Carbon*, 2008, **46**, 229-235.

30 L. Wang, H. R. Byon, *J. Power Sources.*, 2013, **236**, 207-214.

31 N. Tachikawa, K. Yamauchi, E. Takashima, J.-W. Park, K. Dokko, M. Watanabe, *Chem. Commun.*, 2011, **47**, 8157-8159.